

AD-A123 643

NONUNIFORMITIES IN LASER-ABLATED PLASMA(U) NAVAL
RESEARCH LAB WASHINGTON DC M J HERBST ET AL 30 DEC 82
NRL-MR-4983

1/1

UNCLASSIFIED

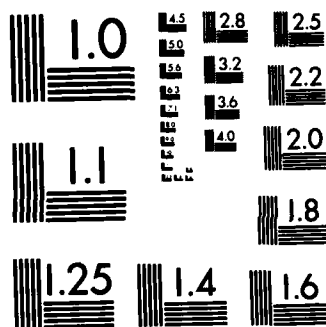
F/G 20/5

NL

END

FILMED

DTIC



MICROCOPY RESOLUTION TEST CHART
NATIONAL BUREAU OF STANDARDS-1963-A

ADA 123643

SECURITY CLASSIFICATION OF THIS PAGE (When Data Entered)

REPORT DOCUMENTATION PAGE		READ INSTRUCTIONS BEFORE COMPLETING FORM
1. REPORT NUMBER NRL Memorandum Report 4983	2. GOVT ACCESSION NO. AD-A223643	3. RECIPIENT'S CATALOG NUMBER
4. TITLE (and Subtitle) NONUNIFORMITIES IN LASER-ABLATED PLASMA		5. TYPE OF REPORT & PERIOD COVERED
7. AUTHOR(s) M. J. Herbst, J. A. Stamper, R. H. Lehmberg, R. R. Whitlock, F. C. Young, J. Grun,* and B. H. Ripin		6. PERFORMING ORG. REPORT NUMBER
9. PERFORMING ORGANIZATION NAME AND ADDRESS Naval Research Laboratory Washington, DC 20375		8. CONTRACT OR GRANT NUMBER(s)
11. CONTROLLING OFFICE NAME AND ADDRESS U.S. Department of Energy Washington, DC 20545		10. PROGRAM ELEMENT, PROJECT, TASK AREA & WORK UNIT NUMBERS DOE AI08-79DP 40092(172) 47-0859-0-2
14. MONITORING AGENCY NAME & ADDRESS (if different from Controlling Office)		12. REPORT DATE December 30, 1982
		13. NUMBER OF PAGES 12
		15. SECURITY CLASS. (of this report) UNCLASSIFIED
		15a. DECLASSIFICATION/DOWNGRADING SCHEDULE
16. DISTRIBUTION STATEMENT (of this Report) Approved for public release; distribution unlimited.		
17. DISTRIBUTION STATEMENT (of the abstract entered in Block 20, if different from Report)		
18. SUPPLEMENTARY NOTES *Present address: Mission Research Corporation, Alexandria, VA 22312 This paper was prepared for presentation at the First Topical Conference on Symmetry Aspects of Inertial Fusion Implosions held at the Naval Research Laboratory, Washington, DC on May 27-28, 1981.		
19. KEY WORDS (Continue on reverse side if necessary and identify by block number) Self-focusing Filamentation Plasma diagnostics Plasma instabilities		
20. ABSTRACT (Continue on reverse side if necessary and identify by block number) With long pulse-duration (4 nsec), moderate intensity ($\sim 10^{13}$ W/cm ²) Nd-laser illumination of planar targets, evidence is found in images of x-ray, $3/2\omega_0$ and $2\omega_0$ emission for filamentation of the incident beam. Calculations indicate that this may be due to thermal self-focusing of hot spots in the laser. X-ray images show spots and spicules, jets of material flow which appear to follow the fluid flow from the target. These may be attributed to the presence of microscopic impurities on our laser-irradiated foil targets.		

DD FORM 1473

1 JAN 73

EDITION OF 1 NOV 65 IS OBSOLETE
S/N 0102-014-6601

SECURITY CLASSIFICATION OF THIS PAGE (When Data Entered)



NONUNIFORMITIES IN LASER-ABLATED PLASMA*

M. J. HERBST, J. A. STAMPER, R. H. LEHMBERG, R. R. WHITLOCK, F. C. YOUNG,
J. GRUN[†], AND B. H. RIPIN

U.S. Naval Research Laboratory,
Washington, D.C. 20375

CLASS	
SECRET	<input checked="" type="checkbox"/>
NO. 1	<input type="checkbox"/>
NO. 2	<input type="checkbox"/>
NO. 3	<input type="checkbox"/>
NO. 4	<input type="checkbox"/>
NO. 5	<input type="checkbox"/>
NO. 6	<input type="checkbox"/>
NO. 7	<input type="checkbox"/>
NO. 8	<input type="checkbox"/>
NO. 9	<input type="checkbox"/>
NO. 10	<input type="checkbox"/>
NO. 11	<input type="checkbox"/>
NO. 12	<input type="checkbox"/>
NO. 13	<input type="checkbox"/>
NO. 14	<input type="checkbox"/>
NO. 15	<input type="checkbox"/>
NO. 16	<input type="checkbox"/>
NO. 17	<input type="checkbox"/>
NO. 18	<input type="checkbox"/>
NO. 19	<input type="checkbox"/>
NO. 20	<input type="checkbox"/>
NO. 21	<input type="checkbox"/>
NO. 22	<input type="checkbox"/>
NO. 23	<input type="checkbox"/>
NO. 24	<input type="checkbox"/>
NO. 25	<input type="checkbox"/>
NO. 26	<input type="checkbox"/>
NO. 27	<input type="checkbox"/>
NO. 28	<input type="checkbox"/>
NO. 29	<input type="checkbox"/>
NO. 30	<input type="checkbox"/>
NO. 31	<input type="checkbox"/>
NO. 32	<input type="checkbox"/>
NO. 33	<input type="checkbox"/>
NO. 34	<input type="checkbox"/>
NO. 35	<input type="checkbox"/>
NO. 36	<input type="checkbox"/>
NO. 37	<input type="checkbox"/>
NO. 38	<input type="checkbox"/>
NO. 39	<input type="checkbox"/>
NO. 40	<input type="checkbox"/>
NO. 41	<input type="checkbox"/>
NO. 42	<input type="checkbox"/>
NO. 43	<input type="checkbox"/>
NO. 44	<input type="checkbox"/>
NO. 45	<input type="checkbox"/>
NO. 46	<input type="checkbox"/>
NO. 47	<input type="checkbox"/>
NO. 48	<input type="checkbox"/>
NO. 49	<input type="checkbox"/>
NO. 50	<input type="checkbox"/>
NO. 51	<input type="checkbox"/>
NO. 52	<input type="checkbox"/>
NO. 53	<input type="checkbox"/>
NO. 54	<input type="checkbox"/>
NO. 55	<input type="checkbox"/>
NO. 56	<input type="checkbox"/>
NO. 57	<input type="checkbox"/>
NO. 58	<input type="checkbox"/>
NO. 59	<input type="checkbox"/>
NO. 60	<input type="checkbox"/>
NO. 61	<input type="checkbox"/>
NO. 62	<input type="checkbox"/>
NO. 63	<input type="checkbox"/>
NO. 64	<input type="checkbox"/>
NO. 65	<input type="checkbox"/>
NO. 66	<input type="checkbox"/>
NO. 67	<input type="checkbox"/>
NO. 68	<input type="checkbox"/>
NO. 69	<input type="checkbox"/>
NO. 70	<input type="checkbox"/>
NO. 71	<input type="checkbox"/>
NO. 72	<input type="checkbox"/>
NO. 73	<input type="checkbox"/>
NO. 74	<input type="checkbox"/>
NO. 75	<input type="checkbox"/>
NO. 76	<input type="checkbox"/>
NO. 77	<input type="checkbox"/>
NO. 78	<input type="checkbox"/>
NO. 79	<input type="checkbox"/>
NO. 80	<input type="checkbox"/>
NO. 81	<input type="checkbox"/>
NO. 82	<input type="checkbox"/>
NO. 83	<input type="checkbox"/>
NO. 84	<input type="checkbox"/>
NO. 85	<input type="checkbox"/>
NO. 86	<input type="checkbox"/>
NO. 87	<input type="checkbox"/>
NO. 88	<input type="checkbox"/>
NO. 89	<input type="checkbox"/>
NO. 90	<input type="checkbox"/>
NO. 91	<input type="checkbox"/>
NO. 92	<input type="checkbox"/>
NO. 93	<input type="checkbox"/>
NO. 94	<input type="checkbox"/>
NO. 95	<input type="checkbox"/>
NO. 96	<input type="checkbox"/>
NO. 97	<input type="checkbox"/>
NO. 98	<input type="checkbox"/>
NO. 99	<input type="checkbox"/>
NO. 100	<input type="checkbox"/>

ABSTRACT

With long pulse-duration (4 nsec), moderate intensity ($\approx 10^{13}$ W/cm²) Nd-laser illumination of planar targets, evidence is found in images of x-ray, $3/2 \omega_0$ and $2\omega_0$ emission for filamentation of the incident beam. Calculations indicate that this may be due to thermal self-focusing of hot spots in the laser. X-ray images show spots and spicules, jets of material flow which appear to follow the fluid flow from the target. These may be attributed to the presence of microscopic impurities on our laser-irradiated foil targets.

NOTE: This manuscript has been revised in proof to include information, as indicated in Sec. IV, that was not available at the time of the oral conference presentation. This information is also contained in a published erratum.¹⁴

Distribution/
Availability Codes
Available and/or
Special

A

I. INTRODUCTION

High compression of laser-fusion pellets requires application of a uniform pressure at the pellet surface.¹ While driving-pressure symmetry can be enhanced due to lateral energy flow during transport between the absorption region and the pellet surface,^{1,2} it is certainly desirable for the laser illumination in the absorption region to be as uniform as possible. As presently envisioned, multimillimeter-diameter pellets will be irradiated by multiananosecond pulses in laser fusion reactors. In the large plasma atmospheres that will result, thermal^{3,6} or ponderomotive^{3,7-10} effects may lead to self-focusing or filamentation of the incident laser beam, thereby seriously degrading illumination uniformity. In addition, other effects that are deleterious to laser fusion (e.g., fast electron generation) may be driven locally by the higher laser intensity present in the filaments.

To simulate the large plasma atmosphere of a reactor pellet, 50-300 Joule pulses from the Pharos II Nd-laser¹¹ ($\lambda = 1.054 \mu\text{m}$, $\tau_L = 3-4$ nsec) are

focused to large spot diameter (0.6-1.0 mm) on planar targets of polystyrene (CH) or aluminum. Large underdense plasmas (lengths near 1 mm, with density gradient scalelengths near $n_e = 0.1 n_c$ in excess of $100 \mu\text{m}^2$) are thereby created. Images of second harmonic ($2\omega_0$) and three-halves subharmonic ($3/2 \omega_0$) emissions provide evidence for filamentation;¹³ these are discussed in Sec. III. X-ray images show spots¹³ and spicules,¹⁴ jets of material flowing from the target surface. These may be attributed to the presence of microscopic, higher-Z impurities on the low-Z foil targets.

II. EXPERIMENTAL DESCRIPTION

As stated in the introduction, planar targets of CH or Al are illuminated with 50-300 J of Nd-laser ($\lambda = 1.054 \mu\text{m}$, $\tau_L = 3-4$ nsec) radiation. In the quasi-near-field of an f/7 input lens, spot diameters (50% energy content) between 0.6 and 1.0 mm are irradiated with incident intensities $I_0 \approx 0.1-1 \times 10^{13}$ W/cm². Targets are tilted by 6° relative to the incident beam direction so as to deflect specular reflections from the incident lens cone. Incident beam polarizations are either circularly or p-polarized; since no major differences are found in the results for these two polarizations, no further mention of polarization state will be made.

Manuscript approved November 2, 1982

[†]Mission Research Corporation, Alexandria, VA

*Work supported by the U.S. Department of Energy and Office of Naval Research

The experimental arrangement is schematically shown in Fig. 1. Visible emission is collected parallel to the target surface by an $f/2$ lens and imaged through narrow band filters onto Polaroid positive-negative film (for $2\omega_0$) or Kodak type I-N spectroscopic plates (for $3/2 \omega_0$). These images, obtained with the "2-D camera" of Fig. 1, yield time-integrated information with two degrees of spatial resolution. A Wollaston prism in the imaging path causes slight degradation in focal sharpness, but allows simultaneous, independent imaging in two polarizations of emitted light. This enhances contrast of polarized harmonic emission over unpolarized continuum emission. Time-resolved information can also be obtained by imaging a fraction of the emission onto the slit of a streak camera, though only one spatial dimension is resolved in these streak images.

EXPERIMENTAL APPARATUS

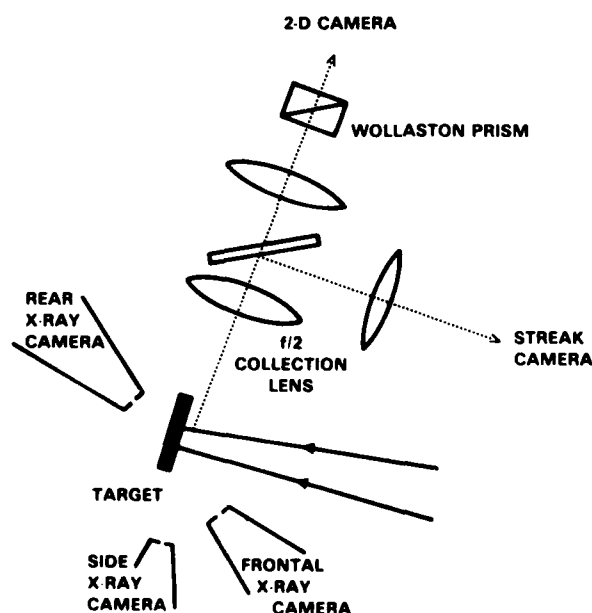


Fig. 1 — Experimental schematic, showing imaging systems for visible and x-ray emission. All visible imaging was done from the side.

Time-integrated images of x-ray emission from these targets are obtained from a range of angles, as shown in Fig. 1. Both frontal and rear pinhole cameras detect emission from the laser-irradiated front side of the target, though the rear camera looks only at emission which is transmitted through the target material. All cameras are equipped with nominally $18 \mu\text{m}$ thick beryllium

filters, so that images are of photons with energy $h\nu \geq 1 \text{ keV}$.

III. EVIDENCE FOR FILAMENTATION

In the present work, experimental evidence is found for four signatures of filamentation: (1) localization on a finer spatial scale than incident beam nonuniformities, (2) locally lower density in these regions, (3) locally higher laser intensity in these regions, with an increase in intensity modulation over that present in the incident beam, and (4) the appearance of these effects only at higher incident intensity. Previous^{15,16} and concurrent^{17,18} investigations provide evidence for some of these properties; the simultaneous inference of all four in this work allows a stronger case to be made for the presence of filamentation.

A. Uniformity of the Incident Beam

We must characterize the nonuniformity of the focused incident beam in order to recognize changes in the intensity distribution which are caused by interaction with the plasma. In Fig. 2B is shown an example of one isointensity contour from a series of contours which is obtained on bismuth-coated glass slides in an equivalent focal plane on every target shot. Large scale structure in the focal distribution is seen in the form of linear fringes with $100\text{--}200 \mu\text{m}$ spacing; inspection of the entire series of isointensity images suggests a peak-to-trough intensity modulation level near 2:1 for this structure. Interestingly, this pattern is also observed in x-ray images as obtained with the rear pinhole camera, as shown in Fig. 2A.

The finest structure observed in laser focal images has $50\text{--}80 \mu\text{m}$ spatial scale and peak intensities in these hot spots may be up to twice the average intensity; while even finer structure may exist, it must have significantly lower modulation level. Finer scale structure observed in x-ray images, as best illustrated by Fig. 2C, was previously believed¹³ to provide evidence for more localized regions of higher laser intensity; however, we now have evidence, as discussed in Sec. IV, for the presence of microscopic, high-Z impurities in our low-Z target foils. While we cannot state with certainty that all of the fine scale structure observed in x-ray images such as Fig. 2C is due to these impurities, their presence precludes our use of such x-ray images as evidence for laser intensity modulation. The most direct evidence for filamentation is based upon the visible observations discussed in Sec. III B.

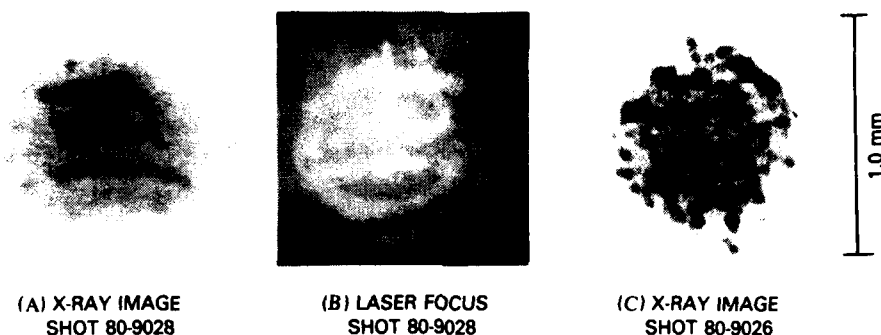


Fig. 2 — (A) Rear-side x-ray image for 12.5 μm Al foil target at $I_0 \approx 2.9 \times 10^{12} \text{ W/cm}^2$; (B) laser focal isointensity contour from same shot as (A); (C) Rear side x-ray image for 7 μm Al foil target at $I_0 \approx 3.4 \times 10^{12} \text{ W/cm}^2$.

B. Visible Observations

As the incident intensity is increased, time-integrated images of emitted light at the second harmonic ($2\omega_0$) and three-halves subharmonic ($3/2 \omega_0$) reveal that emission first occurs from filamentary-appearing regions, with complete surfaces of emission (presumably the $n_c/4$ surface for $3/2 \omega_0$ and the n_c surface for $2\omega_0$) appearing only at higher incident intensity. Near threshold for detection of $3/2 \omega_0$ radiation (average intensity $I_0 \approx 5.6 \times 10^{12} \text{ W/cm}^2$), filamentary structures as in Fig. 3A are seen in both emitted light polarizations. These filaments have transverse dimensions of 5-15 μm and lengths greater than 200 μm . As I_0 is increased by a factor of 2, $3/2 \omega_0$ emission from the entire $n_c/4$ surface is detected; this emission appears first on the downstream (laser) side of the filaments, but is quite broad in extent along the laser direction. Two lobes of emission are observed in images of $3/2 \omega_0$ with polarization corresponding to the laser (Fig. 3B); curiously, a different image is obtained in the orthogonal polarization (Fig. 3C).

With $I_0 \geq 2.8 \times 10^{12} \text{ W/cm}^2$, filamentary structures are also found in time-integrated images of $2\omega_0$ emission, as seen in Fig. 4. The large region of uniform exposure is visible continuum, as verified by substitution of filters which exclude $2\omega_0$; only the filaments along the laser axis are unique to $2\omega_0$. The filaments have lengths along the laser axis of up to 125 μm , transverse dimensions of 5-15 μm , and are observed only in images with polarization corresponding to the incident laser. With a factor of 4 increase in I_0 , parts of a well-defined surface of $2\omega_0$ emission appear at the downstream end of the filaments.

Inference of Local Intensity Modulation. From the transverse modulation of the $3/2 \omega_0$ emission,

we infer the presence of localized regions of higher laser intensity, with an intensity modulation level at least as large as that present in the incident beam. As a complete surface of $3/2 \omega_0$ emission is observed at twice the intensity at which the filaments are first seen, one might infer that the intensity in the filaments is twice that in the surrounding beam. However, the conversion efficiency of light from ω_0 to harmonics is a function of density gradient scalelength $L_n = (n_e^{-1} dn_e/dx)^{-1}$, as well as of laser intensity. The efficiency of conversion from ω_0 to $3/2 \omega_0$ increases monotonically with density gradient scalelength¹⁹⁻²¹ (at least until scalelengths become so long that inverse bremsstrahlung reduces the amount of light reaching the $n_c/4$ region²¹). As one would expect localized structures to have shorter scalelengths than the rest of the blowoff, the $3/2 \omega_0$ production would be reduced, if anything, for a given incident intensity in the observed channels. We may then estimate a lower bound for the intensity modulation at $n_c/4$ by assuming that L_n in the filaments and in the remainder of the blowoff are equal; this lower bound is the 2:1 intensity modulation level mentioned above. The lower bound is the same as the intensity modulation level in the incident beam, but there is now a finer spatial scale.

Similar analysis of the $2\omega_0$ images yields an intensity modulation at n_c of 4:1, as parts of a surface are seen at 4 times the incident intensity at which the filaments are seen. Theoretically, the dependence of $2\omega_0$ generation on L_n is nonmonotonic, however, maximizing at density gradient scalelengths of several wavelengths.^{22,24} Since it is possible, therefore, to have enhanced $2\omega_0$ generation due to shorter L_n , it is not clear whether the inferred intensity modulation is an overestimate or underestimate. A 4:1 modulation would certainly

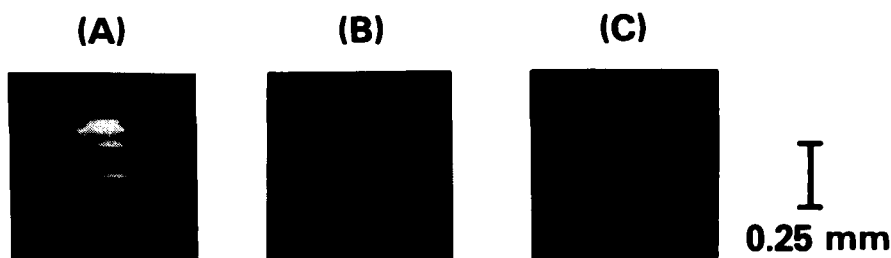


Fig 3 — $3/2 \omega_0$ images for CH targets: (A) central region of 1 mm laser spot on $40 \mu\text{m}$ thick foil at $I_0 \approx 6.1 \times 10^{12} \text{ W/cm}^2$; (B) $42.7 \mu\text{m}$ thick, $500 \mu\text{m}$ diameter disk at $I_0 \approx 1.1 \times 10^{13} \text{ W/cm}^2$, with emitted light polarization corresponding to incident laser; and (C) same shot as (B), but with orthogonal polarization. Laser is incident from left in all images.

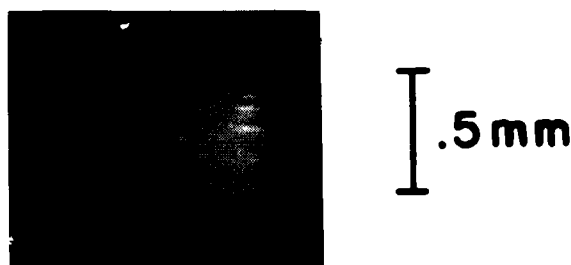


Fig. 4 — $2\omega_0$ image for $7 \mu\text{m}$ CH target at $I_0 \approx 6.1 \times 10^{12} \text{ W/cm}^2$. Laser is incident from left, and dark vertical edge at right is target surface. General exposure due to emitted continuum is seen in addition to filaments of emitted $2\omega_0$.

represent an increase over the modulation present on the incident beam.

Mechanisms That Can Spuriously Cause Filamentary Appearance. Although it is tempting to point to the filamentary appearance of the emitting regions as evidence for filamentation, there are at least three alternative mechanisms for explaining this appearance. First, since the images are time-integrated, target motion due to ablative acceleration²⁵ during the period of emission could result in an axial smearing in the images. This is easily eliminated by using thicker targets which do not move.

Even with a stationary target, however, the $n_c/4$ and n_c density surfaces may move as the blowoff plasma profile evolves. To determine whether this effect is important, streak images of the emitted light are obtained, using the setup described in Sec. II. A direct test for motion of the n_c surface, through streak photography of the $2\omega_0$ emission, is not possible, since the poor contrast of

the $2\omega_0$ emission over emitted continuum prevents distinguishing between the two emissions without two spatial dimensions of resolution (one spatial dimension must be sacrificed for time resolution in streak imaging). We do directly test, through $3/2 \omega_0$ streak photography, for motion of the $n_c/4$ surface, as shown in Fig. 5. At any given instant of time, the extent of the emitting region along the laser axis can be quite large, up to $250 \mu\text{m}$. The position of strongest $3/2 \omega_0$ emission is nearly stationary for the entire emitting period, approximately 2 nsec in this case. Hence, the effect of $n_c/4$ surface motion on filament lengths is negligible. Since the target motion is also negligible, we feel that the motion of the n_c surface, located between the two, is likely to be unimportant. A temporal modulation (approximately 200 ps period), as observed in the emission of Fig. 5, is not uncommon, and is not believed to be present in the incident laser pulse; we have no definite explanation for this modulation, which is reminiscent of earlier results at KMS²⁶ and Rutherford²⁷ using shorter laser pulses at higher incident intensity.

The third mechanism which can spuriously cause the filamentary appearance of the visible images is refraction. Refraction of the emitted light as it exits the blowoff plasma can lead to lengthening of the observed image, since rays emitted from a point into different angles are bent differently and appear to originate from different sources. This is illustrated in Fig. 6A. Refracted ray paths are calculated for point sources at $n_c/4$ (for $3/2 \omega_0$) and n_c (for $2\omega_0$) in a plane-stratified plasma with an exponential density profile. For $L_n = 100\text{--}125 \mu\text{m}$ at $n_c/4$, the observed length of $3/2 \omega_0$ structures could be explained solely by refraction. The double-lobe pattern of Fig. 3B may also be a signature of refraction. For a certain range of L_n , a single source may emit two isolated sets of rays (one

NONUNIFORMITIES IN LASER-ABLATED PLASMA



Fig. 5 — Streak photograph of $3/2 \omega_0$ emission from $70 \mu\text{m}$ thick CH target at $I_0 \approx 7.2 \times 10^{12} \text{ W/cm}^2$. Filaments are observed in 2-D image of $3/2 \omega_0$ on same shot. Image of target is orthogonal to streak camera slit, so the one dimension of spatial resolution, labeled z in the figure, is approximately the axis of the incident beam. Laser is incident from right, and target position is approximately at $z = 0$. Time increases upwards and $t = 0$ in the figure is arbitrary, though this emission is occurring during the peak intensity of the incident pulse.

POSSIBLE REFRACTIVE EFFECTS ON IMAGES OF VISIBLE EMISSION

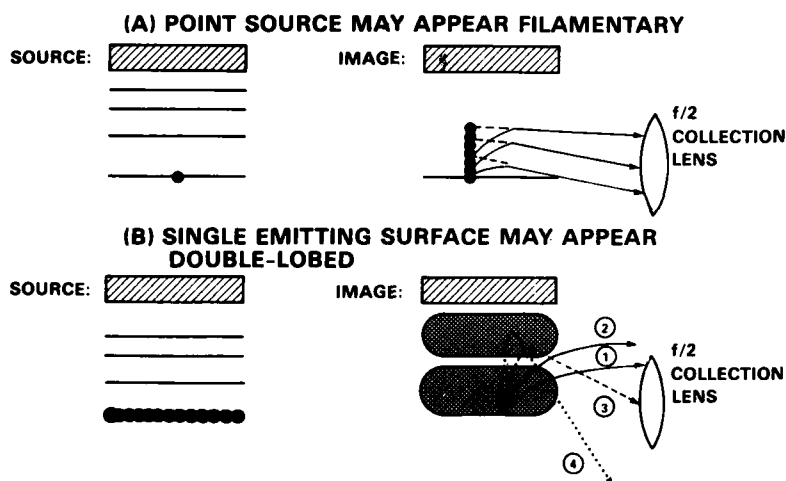


Fig. 6 — An illustration of the possible difference, due to refraction, between filaments and filamentary-appearing structures. The hatched rectangle is the target, the horizontal lines below the target are isodensity contours, and the laser is incident from below for all of the illustrations. (A) On the left, we show a point source of $2\omega_0$ on the n_c contour or of $3/2 \omega_0$ on the $n_c/4$ contour. On the right, the paths of rays of harmonic emission which has been emitted into a range of angles are shown. The bending within the plasma of rays that are collected by the $f/2$ lens leads to a locus of apparent source points on the image which resemble a filament. (B) Here, the effect of refraction on emission from a complete surface, as shown on the left, is examined. For a certain range of density gradient scalelengths, one can obtain the family of ray paths numbered 1-4. Ray 1, emitted near 90° to the incident laser direction, is bent somewhat but still collected by the $f/2$ lens. Rays such as 2, emitted slightly closer to the target normal, are not refracted enough to be collected. At still steeper angle of emission, ray 3 penetrates to higher density, is refracted more strongly, and is collected by the lens. Finally, ray 4 and other rays emitted near the target normal are refracted too strongly to be collected. The apparent source, due to rays near 1 and 3, is two lobes of emission separated by an apparently nonemitting region. This may explain the appearance of Fig. 3B.

near 90° and one propagating toward critical density, as shown in Fig. 6B) which bend into the $f/2$ collection cone. Refraction does not, however, explain the difference at higher I_0 between images with the two polarizations (Fig. 3B vs 3C). One possibility is that two production mechanisms operate in different regions of the plasma, with each responsible for one of the observed polarizations. Lengths of $2\omega_0$ images could also be explained by refraction, though this requires an $L_n \geq 200 \mu\text{m}$, much larger than expected at n_c . Additionally, when the $2\omega_0$ surface appears, it has a much smaller axial extent than the filaments, implying that refraction is not the sole cause of $2\omega_0$ filament length.

Inference of Locally Lower Density. It appears, then, that $2\omega_0$ filament lengths are likely to be real, though refraction may be enhancing the lengths observed for $3/2\omega_0$ structures. If the $2\omega_0$ filaments are real, lower density may be inferred in the channels; this also applies for $3/2\omega_0$ if filament lengths are not due to refraction. The appearance of the $3/2\omega_0$ and $2\omega_0$ surfaces on the *downstream* side of the filaments implies that the $n_c/4$ and n_c surfaces are perturbed locally toward higher density regions, as by a low density channel (see Fig. 7B). A high density channel, as in Fig. 7A, would perturb the surfaces toward lower density, and they would be seen *upstream* of the filaments. Therefore, visible observations do imply higher intensity and lower density, as for filamentation, in regions more localized than laser hot spots. That this only occurs at higher I_0 would also be consistent with filamentation, but could be due to the threshold for production of the harmonic emission itself.

C. Calculated Growth of Filamentation

Optical filamentation in plasmas can generally arise from both thermal³⁻⁶ and ponderomotive^{3,7-10} mechanisms. Under the experimental conditions described here, these components can have comparable magnitudes, although the thermal part will tend to predominate in higher Z targets. The following calculations will therefore include both effects, and will examine the applicability of the theory³⁻¹⁰ to the present experiments.

The calculations will proceed from three main assumptions: (a) the filamentation is quasi-steady-state, (b) the plasma parameters vary slowly in distances comparable to filamentation growth lengths, and (c) the electron density variations $n(r) - n_0$ induced by the beam inhomogeneity remain small. Assumption (a) is justified if both the ion-acoustic transit time and thermal diffusion time across the filament remain short in comparison to the optical pulsewidth. Although assumption (b) is not fully satisfied under the present experimental conditions (plasma scalelengths beyond $n_c/4$ are on the order of one hundred microns), the calculated growth lengths are expected to be a reasonable first approximation. Assumption (c) precludes any consideration of the saturation effects discussed by Sodha, et al.,⁵ and effectively limits the theory to a perturbation treatment. Within these constraints, the optical behavior of the plasma is described by the refractive index

$$\bar{n} = (1 - n/n_c)^{1/2} \approx \epsilon_0^{1/2} + 1/2 \bar{n}_2 |E|^2, \quad (1)$$

where $\epsilon_0 = 1 - n_0/n_c$ is the linear plasma dielectric constant, E is the optical field amplitude, and \bar{n}_2 is the nonlinear refractive index

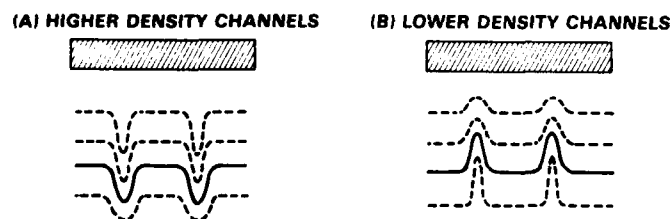


Fig. 7 — Illustration of the method used to infer that harmonic images imply lower density. Target is hatched rectangle, laser is incident from below, and lines correspond to isodensity contours. Solid line corresponds to emitting surface (n_c for $2\omega_0$ or $n_c/4$ for $3/2\omega_0$). (A) The effect of high-density channels is to locally perturb isodensity surfaces toward lower density regions. (B) Conversely, lower density channels perturb isodensity surfaces inward, toward the target. This corresponds to the relative orientation of filaments and surfaces experimentally observed in the images.

$$\bar{n}_2 = 2d\bar{n}/d|E|^2 = -(1/n_e \epsilon_0^{1/2}) dn/d|E|^2. \quad (2)$$

Filamentation in a nonlinear medium described by Eq. (1) has been treated theoretically by many authors.^{28,6,7} The basic approach is to calculate the longitudinal growth rate $\alpha(k_1)$ of a small transverse (x) periodic perturbation

$$E_1(x, z) = E_+(z) e^{ik_1 x} + E_-(z) e^{-ik_1 x},$$

superimposed on a large plane wave $E_0(z)$. Substituting the total amplitude $E = E_0 + E_1$ into the optical wave equation, one obtains the general expression²⁸

$$\alpha(k_1) = \left[(k_1^2 \bar{n}_2 |E_0|^2 / 2\epsilon_0^{1/2}) - (k_1^2 / 2k_0) \right]^{1/2}, \quad (3)$$

where $k_0 = \epsilon_0^{1/2} \omega_0 / c$.

The expression for \bar{n}_2 must now be calculated from the plasma momentum and energy conservation equations, including ponderomotive force and collisional absorption. Expressing the electron density n , blowoff velocity \bar{u} , and electron (ion) temperature T_e (T_i) in terms of their quasi-equilibrium values, plus the periodic transverse perturbations,

$$n = n_0 + n_1(x, z), \quad \bar{u} = \bar{u}_0 + \bar{u}_1(x, z)$$

$$T_e = T_{e0} + T_1(x, z), \quad T_i = T_0 \lesssim T_{e0},$$

one obtains the linearized steady state momentum equation

$$\begin{aligned} 2(n_0/Z) m_i \bar{u}_0 \cdot \nabla \bar{u}_1 = \\ - (T_{e0} + T_0/Z) \nabla n_1 - n_0 \nabla T_1 \\ - (n_0 / 16 \pi n_c) \nabla |E|^2, \end{aligned} \quad (4)$$

where $|E|^2 \equiv E_0^* E_1 + E_0 E_1^*$. The steady state equation is justified for the conditions of interest ($T_0 \approx 400$ eV and $\lambda_1 = 2\pi/k_1 \approx 50 \mu\text{m}$), where the acoustic velocity c_s is of order 2×10^7 cm/sec, and the transit time is of order $(k_1 c_s)^{-1} \approx 40$ psec. In the region near the center of the beam (where most of the filamentation is observed), the blowoff is nearly longitudinal; hence, one can take $\bar{u}_0 \cdot \nabla \bar{u}_1 \approx 0$. Equations (4) and (2) then yield the result

$$\bar{n}_2 = \bar{n}_{2P} + \bar{n}_{2T}, \quad (5)$$

where \bar{n}_{2P} and \bar{n}_{2T} are, respectively, the ponderomotive and thermal contributions

$$\bar{n}_{2P} = \frac{n_0 n_c}{16 \pi (1 + 1/Z) \epsilon_0^{1/2} n_c T_0}, \quad (6a)$$

$$\bar{n}_{2T} = \frac{n_0 n_c}{(1 + 1/Z) \epsilon_0^{1/2} T_0} \frac{dT_1}{d|E|^2}, \quad (6b)$$

and we have approximated $T_{e0} \approx T_0$.

The expression for $dT_1/d|E|^2$ can now be found from the linearized electron heat equation

$$\begin{aligned} \nabla \cdot \bar{q}_1 + n_0 T_0 \nabla \cdot \bar{u}_1 \\ + (2m_e/m_i) \nu_e \cdot (3/2) n_0 T_1 \\ = \nu_e n_0 |E|^2 / 8 \pi n_c, \end{aligned} \quad (7)$$

where \bar{q}_1 is the thermal flux perturbation, and

$$\nu_e = 5.90 \times 10^{-24} \ln \Lambda Z n_0 / T_0^{3/2} \text{ (cgs)} \quad (8)$$

is the electron-ion collision rate.²⁹ The convection term, which is proportional to $\bar{u}_0 \cdot \nabla T_1$, has been neglected for a reason similar to that given in the preceding paragraph for neglecting $\bar{u}_0 \cdot \nabla \bar{u}_1$.

Following earlier treatments,^{5,6} we now assume that \bar{q}_1 can be described classically,³⁰ i.e.,

$$\bar{q}_1 = -K \nabla T_1, \quad (9a)$$

$$K = 5.98 \times$$

$$10^{50} T_0^{5/2} \phi(Z) / Z \ln \Lambda, \text{ (cgs)} \quad (9b)$$

where $\phi \approx (Z + .24) / (1 + .24Z)$. However, according to Bell, Evans and Nicholas,³¹ such a description will be adequate only if $|\nabla T_1| < T_0 / 30 \lambda_e$, where $\lambda_e = (T_0 / m_e)^{1/2} \nu_e^{-1}$ is the electron mean free path. For $T_0 \approx 400$ eV, $n_0 = n_c / 4$, and $\lambda_1 = 50 \mu\text{m}$, one finds $\lambda_e \approx 11.5/Z$ micron; hence, the classical description requires $|T_1| / T_0 < Z/40$, which is consistent only with a perturbation treatment.

One can now show that the thermal diffusion time, along with the compression and electron-ion relaxation terms of Eq. (7), are negligible under the above considerations. The diffusion time Δt can be estimated from the relation $(\nu_e \Delta t)^{1/2} \lambda_e \approx k_1^{-1}$, giving the result $\Delta t \approx (2.5)Z$ psec. The compression/conduction ratio can be estimated from (9a,b):

$$\frac{|n_0 T_0 \nabla \cdot \bar{u}_1|}{|K \nabla^2 T_1|} \approx \left(\frac{m_e}{m_i} \right)^{1/2} (k_1 \lambda_e)^{-1} \ll 1.$$

Finally, the relaxation/conduction ratio is

$$\frac{|3(m_e/m_i) \nu_e n_0 T_1|}{|K \nabla^2 T_1|} \approx \frac{m_e}{m_i} (k_1 \lambda_e)^{-2} \ll 1$$

Under the conditions of interest Eq. (7) thus reduces to the form^{5,6}

$$-K \nabla^2 T_1 = K k_1^2 T_1 = \nu_e n_0 |E|^2 / 8 \pi n_c, \quad (10)$$

which gives the thermal nonlinear index

$$\bar{n}_{2T} = \frac{(n_0 n_c)^2 \nu_e}{8 \pi (1 + 1/Z) \epsilon_0^{1/2} k_1^2 K T_0} \quad (11)$$

when substituted into expression (6b). The relative magnitude of the two indices is

$$\bar{n}_{2T}/\bar{n}_{2P} = 2 n_0 \nu_e / K k_1^2 = .016 \lambda_L^2 / \lambda_e^2 \phi(Z). \quad (12)$$

This ratio is ≈ 1.8 for CH ($Z = 3.5$) and ≈ 16 for Al ($Z = 13$).

Expressions (3), (5), (6a) and (11) can now be combined to give the total longitudinal growth rate

$$\alpha(k_1) = \left[(\alpha_{PM} k_1^2 / k_0) + \alpha_{TM}^2 - (k_1^2 / 2k_0)^2 \right]^{1/2} \quad (13)$$

where

$$\alpha_{PM} = \frac{k_0 \bar{n}_{2P} |E_0|^2}{2 \epsilon_0^{1/2}} = \frac{(n_0/n_c) k_0 I}{4 (1 + 1/Z) \epsilon_0^{3/2} c n_c T_0} \quad (14a)$$

$$= 2.92 \times 10^{-9} \frac{(n_0/n_c) I \text{ (W/cm}^2\text{)} \lambda \text{ (}\mu\text{m)}}{(1 + 1/Z) \epsilon_0 T_0 \text{ (eV)}} \quad (14b)$$

(cm⁻¹)

would be the maximum value of α [occurring when $k_1 = (2k_0 \alpha_{PM})^{1/2}$] if the ponderomotive contribution were acting alone,⁷ and

$$\alpha_{TM} = \left[\frac{\bar{n}_{2T} |E_0|^2}{2 \epsilon_0^{1/2}} \right]^{1/2} k_1 = \left[\frac{(n_0/n_c)^2 \nu_e I}{2 (1 + 1/Z) \epsilon_0^{3/2} c K T_0} \right]^{1/2} \quad (15a)$$

$$= \frac{13.2 \ln \Lambda}{\lambda \text{ (}\mu\text{m)}} \left[\frac{Z^2 (n_0/n_c)^3 I \text{ (W/cm}^2\text{)}}{(1 + 1/Z) \phi(Z) \epsilon_0^{3/2} [T_0 \text{ (eV)}]^5} \right]^{1/2} \quad (15b)$$

(cm⁻¹)

would be the maximum value (occurring when $k_1 = 0$) if the thermal component were acting alone.⁶ One can see physically that as long as steady state conditions prevail, the thermal contribution maximizes as $k_1 \rightarrow 0$ (whole beam self-focusing) because thermal diffusion tends to smear out the shorter λ_L perturbations. On the other hand, transient effects will tend to favor shorter λ_L . Thus, any incident laser hot-spots are likely to grow and produce filaments before whole beam self-focusing can occur.

In view of the present trend toward shorter wavelength fusion drivers, it is worth noting that the thermal contribution α_{TM} increases strongly as λ_0 decreases. This behavior arises not only from the explicit λ_0 dependence, but also from the $T_0^{-5/2}$ term in expression (15b).

The total growth length α^{-1} is plotted vs. $\lambda_L = 2\pi/k_1$ in Fig. 8 for the case of CH and Al targets. For Al targets, the growth is dominated by the thermal self-focusing mechanism; for CH, the

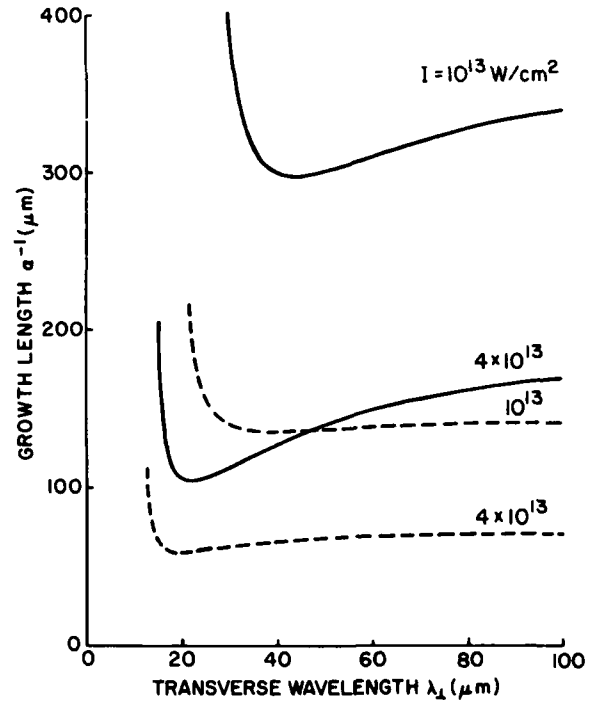


Fig. 8 — Calculated growth lengths α^{-1} vs transverse wavelength λ_L of the perturbation, assuming $n_0 = n_c/4$, $T_0 = 400$ eV and $\lambda = 1.053 \mu\text{m}$. Solid lines pertain to CH ($Z = 3.5$), and dashed lines pertain to Al ($Z = 13$).

thermal effects are approximately twice as important as ponderomotive effects. It is evident that the growth lengths at intensities of the hot spots in the incident beam are short enough to account for the observed filamentation and that, excepting for the cutoff regions where $\alpha \rightarrow 0$, the growth lengths vary slowly with λ_L . Since the filaments grow out of incident hot spots whose λ_L components lie in this range, the slow $\alpha^{-1}(\lambda_L)$ variation suggests that their overall size should not decrease as rapidly as they would if α^{-1} was decreasing as λ_L decreased.

D. Conclusions

A comparison between the expected signatures of filamentation and our experimental observations yields a substantial amount of evidence for the presence of filamentation. Localization is implied by $3/2 \omega_0$ and $2 \omega_0$ images in regions with transverse dimensions less than $15 \mu\text{m}$, as opposed to the $50\text{--}80 \mu\text{m}$ dimensions of incident hot spots. We infer lower density locally from $2 \omega_0$ and perhaps $3/2 \omega_0$ observations, and some evidence of increased intensity modulation over that present in the incident beam is also found. All of these observations apply only at higher incident intensity.

In addition, calculations indicate that thermal self-focusing of hot spots in the incident beam is expected. This large amount of circumstantial evidence leads us to conclude that filamentation is probably occurring. One bright note for laser fusion is that the spatial scale of the intensity variations caused in the absorption region is very fine, much smaller than the expected distance between absorption and ablation regions. Consequently, lateral energy transport between these two regions may well reduce ablation pressure variations to acceptable levels.¹ There may still be deleterious effects of plasma instabilities driven by the higher intensity in the filaments.

IV. OBSERVATION OF SPICULES

As described in Sec. II, side-on images of x-ray emission from the laser-irradiated planar targets are obtained. Approximately half of the pinhole images for CH targets show fine-scale structures projecting well out in front of the target surface, as shown in Fig. 9A. The finest observed transverse dimension of such spicular features is pinhole resolution limited at $12\text{ }\mu\text{m}$. When observed from the target rear at an angle of 45° to the target normal, as shown in Fig. 9B, these spicules appear to emerge from small intense spots near the target surface, as those mentioned in Sec. III.A. On most images, a much larger number of spots than spicules is observed. From many of these spots, short straight filamentary structures emanate; spicules,

which project much further from the target surface, emanate from only a few of the spots.

Another property of these structures is discovered by using thin targets which are ablatively accelerated²⁵ to speeds that allow significant target displacement during the x-ray emission (which has the laser-pulse duration²⁵). Some x-rays emitted from the ablating front surface of the target are then observed as the irradiated section translates through positions behind the original target location (see Fig. 9C). In this image, one observes fine scale striations along the direction of target motion; some of these connect to spicules observed in front of the original target position.

The angle at which a spicule emerges from the blowoff plasma depends upon its position relative to the center of the target. Spicules emanating from source points in the target near the center of the x-ray image propagate at angles near the target normal, while those that emerge from near the edge of the target curve away from the target normal at larger angles.

The spicule orientations suggest that spicules might be following the fluid flow of material from the target surface. To test this hypothesis, an experiment is designed to determine the pattern of material flow from the target.³² Aluminum is locally embedded in $25\text{ }\mu\text{m}$ diameter spots (up to $10\text{ }\mu\text{m}$ deep) within plastic targets, as indicated in

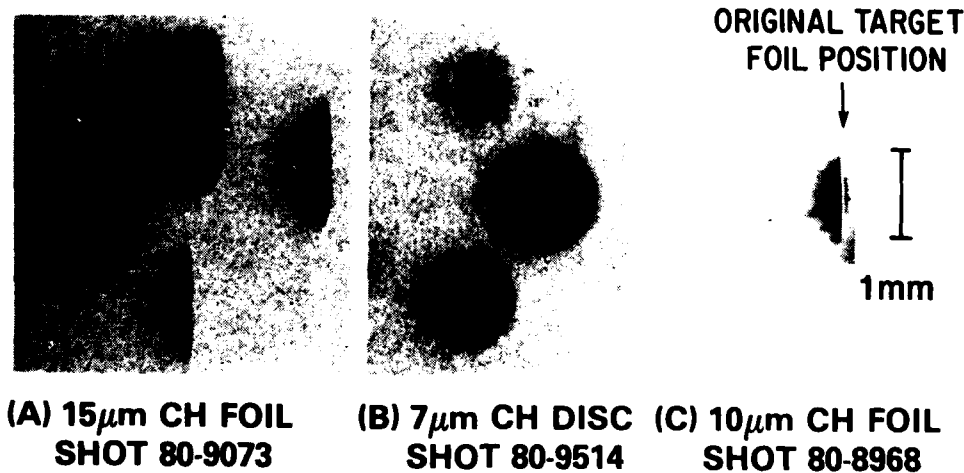


Fig. 9 — (A) Simultaneous side-on images with pinhole diameters between 8 and $55\text{ }\mu\text{m}$. The laser is incident from left with $I_0 \approx 2.8 \times 10^{12}\text{ W/cm}^2$. (B) Images from 45° to rear of disk target. The laser is directed out of the page and 45° to the right with $I_0 \approx 2.8 \times 10^{12}\text{ W/cm}^2$. (C) A side view of an accelerating target at $I_0 \approx 8.3 \times 10^{12}\text{ W/cm}^2$. The laser is incident from the left and some x-rays emanate from the accelerating target behind original foil position. The blackening in the lower right is not part of the image.

Fig. 10. Upon irradiation of this array of spots, the flow of ablated aluminum from each spot can be tracked in side-on x-ray images because of the strong Al x-ray line emission above 1 keV. An example of data obtained in this manner is shown in Fig. 11. The great resemblance of this pattern to the spicule pattern suggests that spicules are following the fluid flow of material from the target.

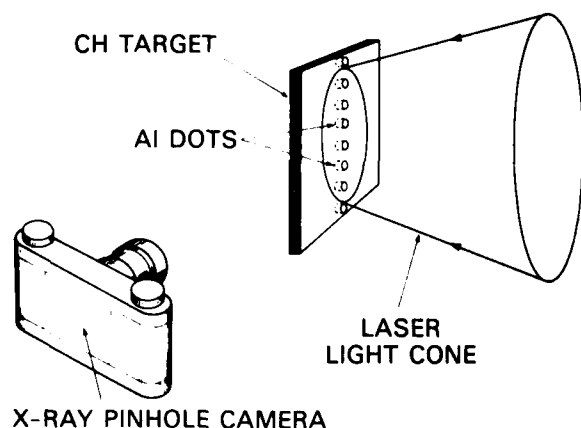


Fig. 10 — Schematic illustration of experimental apparatus used in study of fluid flow of ablated material



Fig. 11 — Example of side-on x-ray image obtained using apparatus of Fig. 10. Laser is incident from left with $I_0 \approx 3.2 \times 10^{12} \text{ W/cm}^2$ and $10 \mu\text{m}$ thick CH target surface is to right. Flow of Al from each spot is observed as dark track (this is a negative image) of stronger x-ray emission flowing to left from the target. Darkening in upper left is part of a separate image.

Spicules may also be observed in images of aluminum targets, though different pinhole camera filtration must be used. The intensity of imaged radiation with the usual Be filters is much greater with Al targets than with CH targets, primarily due to the presence of strong Al line radiation in the spectral band of the camera. The dominant lines in the spectrum are found through crystal-spectrograph measurements to be just above the unionized-Al absorption edge at $h\nu = 1.56 \text{ keV}$. To preferentially filter out these lines, then, is easily accomplished by adding an additional $7 \mu\text{m}$ Al foil filter to the pinhole cameras. Images obtained in this way do show spicules.

Previously,¹⁴ we speculated upon several possible mechanisms to explain the presence of these structures, some of which depended upon the presence of filamentation. Since then, data has been obtained which casts a different light upon our spicule observations. By using an x-ray crystal spectrograph with high spatial resolution, it has been found that the emission spectra of at least some, if not all, of the observed spicules are characteristic of materials of higher atomic number Z than carbon. This result invalidates the implicit assumption in the discussion of possible mechanisms in Ref. 14 that the material in the spicule is the same as that in the blowoff plasma. There, spicules were inferred to have higher density than the surrounding blowoff plasma because they were observed to have higher emissivity and measurements suggested that they had the same color temperature. However, the presence of higher Z plasma renders inappropriate the application of the color temperature analysis and is, in itself, sufficient explanation for the observed higher emissivity. The observation of spicules can be explained, therefore, by the presence of microscopic surface impurities on our laser-irradiated foils, without need for the possible mechanisms outlined in Ref. 14. These impurities are collisionally confined in the spicule, much in the same way as the intentionally introduced tracer materials in Figs. 10 and 11 are confined.

V. CONCLUSION

Through imaging of visible harmonic and subharmonic emissions from laser-irradiated planar targets, evidence is found for filamentation of the incident beam. The fine-scale of the intensity variation in the absorption region, as pointed out in Sec. III, is much less than the expected separation between critical density and the ablation surface; lateral energy transport may then provide the required ablation pressure symmetry at the target surface. Were whole-beam self-focusing to occur, this conclusion would be modified; however, real

laser beams and plasmas have nonuniformities, and filamentation seeded by these is likely to break up the beam before whole-beam effects can grow. The most severe effects of filamentation, then, may be that plasma instabilities driven by the high intensity in the filaments can grow and affect laser-plasma coupling (through reflective instabilities) or fuel preheat (through fast electron generation). Spicule observations, which were previously offered as possible evidence for such an effect of filamentation, are now attributed to the presence of microscopic, higher-Z impurities on our low-Z target foils.

VI. ACKNOWLEDGMENTS

The authors gratefully acknowledge the many good suggestions and ideas offered by S.E. Bodner, J.M. McMahon and S.P. Obenschain of the NRL Laser-Matter Interaction Group. Results of the expert technical assistance of M. Fink, R. McGill, N. Nocerino, L. Seymour, and E. Turbyfill are found throughout this work. Periodic support was also received from R. Prom and A. Unzicker.

REFERENCES

1. J. Nuckolls, L. Wood, A. Thiessen, and G. Zimmerman, *Nature*, **239**, 139 (1972).
2. S.P. Obenschain, B.H. Ripin, E.A. McLean, and J. Grun, NRL Memorandum Report No. 4466 (1981).
3. A.J. Palmer, *Phys. Fluids* **14**, 2714 (1971).
4. F.W. Perkins and E.J. Valeo, *Phys. Rev. Lett.* **32**, 1234 (1974).
5. M.S. Sodha, A.K. Ghatak, and V.K. Tripathi, *Prog. Opt.* **13**, 169 (1976). M.S. Sodha, R.K. Khanna, and V.K. Tripathi, *Opto-Electronics* **5**, 533 (1973).
6. V.K. Tripathi and L.A. Pitale, *J. Appl. Phys.* **48**, 3288 (1977).
7. P. Kaw, G. Schmidt, and T. Wilcox, *Phys. Fluids* **16**, 1522 (1973).
8. J.W. Shearer and J.L. Eddleman, *Laser Light Forces and Self-Focusing in Fully Ionized Plasmas*, *Phys. Fluids* **16**, 10, 1753-61 (1973).
9. J.F. Drake, P.K. Kaw, Y.C. Lee, G. Schmidt, C.S. Liu, and M.N. Rosenbluth, *Phys. Fluids* **17**, 778 (1974).
10. B.I. Cohen and C.E. Max, *Phys. Fluids* **22**, 1115 (1979).
11. J.M. McMahon, R.P. Burns, T.H. DeRieux, R.A. Hunsicker, and R.H. Lehmberg, *IEEE J. Quant. Elect.* **QE17**, 1629 (1981).
12. S.P. Obenschain and J.A. Stamper, private communication.
13. M.J. Herbst, J.A. Stamper, R.R. Whitlock, R.H. Lehmberg and B.H. Ripin, *Phys. Rev. Lett.* **46**, 328 (1981).
14. M.J. Herbst, R.R. Whitlock, and F.C. Young, *Phys. Rev. Lett.* **47**, 91 (1981) and erratum **47**, 1568 (1981).
15. R.A. Haas, H.D. Shay, W.L. Kruer, M.J. Boyle, D.W. Phillion, F. Rainer, V.C. Rupert, and H.N. Kornblum, *Phys. Rev. Lett.* **39**, 1533 (1977).
16. A. Ng, D. Salzmann, A.A. Offenberger, *Phys. Rev. Lett.* **43**, 1502 (1979).
17. H.A. Baldis and P.B. Corkum, *Phys. Rev. Lett.* **45**, 1260 (1980).
18. O. Willi and P.T. Rumsby, *Opt. Comm.* **37**, 45 (1981).
19. C.S. Liu and M.N. Rosenbluth, *Phys. Fluids* **19**, 967 (1976).
20. A.I. Avrov, V. Yu. Bychenkov, O.N. Krokhin, V.V. Pustovalov, A.A. Rupasov, V.P. Silin, G.V. Sklizkov, V.T. Tikhonchuk, and A.S. Shikanov, *Zh. Eksp. Teor. Fiz.* **72**, 970 (1977) [*Sov. Phys. JETP* **45**, 507 (1977)].
21. B. Lasinski, private communication.
22. W.L. Kruer and K.G. Estabrook, in *Laser Interaction and Related Plasma Phenomena*, ed. by H.J. Schwarz and H. Hora (Plenum, New York, 1977), Vol. 4B, p. 709.
23. N.S. Erokhin, V.E. Zakharov, and S.S. Moiseev, *Zh. Eksp. Teor. Fiz.* **56**, 179 (1969). [*Sov. Phys. JETP* **29**, 101 (1969)].
24. N.S. Erokhin, S.S. Moiseev, and V.V. Mukhin, *Nucl. Fusion* **14**, 333 (1974).
25. B.H. Ripin, R. Decoste, S.P. Obenschain, S.E. Bodner, E.A. McLean, F.C. Young, R.R. Whitlock, C.M. Armstrong, J. Grun, J.A. Stamper, S.H. Gold, D.J. Nagel, R.H. Lehmberg, and J.M. McMahon, *Phys. Fluids* **23**, 1012 (1980).
26. T.A. Leonard and R.A. Cover, *J. Appl. Phys.* **50**, 3241 (1979).
27. P.D. Carter, S.M.L. Sim, H.C. Barr, and R.G. Evans, *Phys. Rev. Lett.* **44**, 1407 (1980).
28. V.I. Bespalov and V.I. Talafov, *Pis'ma Zh. Eksp. Teor. Fiz.* **3**, 471 (1966) [*JETP Lett.* **3**, 307 (1966)]. J.H. Marburger, *Laser Induced Damage in Optical Materials*, ed. by A.J. Glass and A.H. Guenther [NBS special publication **356** (1971)] B.R. Suydam, *ibid.* **387** (1973).
29. T.W. Johnston and J.M. Dawson, *Phys. Fluids* **16**, 722 (1973).
30. L. Spitzer, *Physics of Fully Ionized Gases*, 2d rev. ed. (Interscience Publications, John Wiley and Sons, New York, 1962), Sec. 5.5.
31. A.R. Bell, R.G. Evans, and D.J. Nicholas, *Phys. Rev. Lett.* **46**, 243 (1981).
32. M.J. Herbst and J. Grun, *Phys. Fluids* **24**, 1917 (1981).

END

FILMED

2-83

DTIC